PWM Switching Frequency Signal Injection Sensorless Method in IPMSM

Sungmin Kim, *Student Member, IEEE*, Jung-Ik Ha, *Member, IEEE*, and Seung-Ki Sul, *Fellow, IEEE*

Abstract—The rotor position of an interior permanent-magnet synchronous machine (IPMSM) can be estimated without a position sensor by signal injection sensorless control at standstill and/or in very low speed rotating condition. In the signal injection sensorless control, however, the fundamental control performance is limited by the frequency of the injected signal, and no negligible acoustic noise is generated. If the frequency of the injected voltage signal would increase to pulsewidth modulation (PWM) switching frequency and if the switching frequency is near or above audible range, the dynamics of the sensorless control can be improved, and the acoustic noise can be remarkably reduced or totally eliminated. This paper describes how to extract the rotor position information of IPMSM using the voltage signal injection whose frequency is the same as the PWM switching frequency. Compared to the conventional heterodyning process, the proposed method is simple to implement and appropriate for PWM switching frequency signal injection. The high-frequency voltage signal can be injected in the stationary reference frame or in the estimated rotor reference frame. In this paper, the 5- and 16-kHz signal injections are proposed, implemented, and compared. The experimental results confirm the effectiveness of the proposed method.

Index Terms—AC machine, motor drives, sensorless control, signal injection.

I. INTRODUCTION

IN THESE days, the popularity of interior permanent-magnet synchronous machines (IPMSMs) has been increased in many industrial drive systems [1]. The high power density, high torque density, and high efficiency are attractive characteristics of IPMSM for not only conventional drive applications but also high-performance servo applications. Because an IPMSM is a kind of synchronous machines, the rotor position information is essential for field-oriented control [2]. As the result, an encoder or resolver has been attached to the shaft of the rotor. These position sensors invoke many problems: increasing system cost and volume, signal noise issues, and reliability concerns. There-

fore, control techniques which are not dependent on the position sensor have been developed for the last several decades.

In position sensorless control, there are two groups in the sensorless position estimation of IPMSM according to the position estimation principle. One is based on back electromotive force (EMF), and the other uses the magnetic saliency of an IPMSM [3]. In the first group, to extract the rotor position information from the back EMF voltages, it uses voltage models and observers in the synchronous or stationary frame and presents good performance in the middle- and high-speed operations of IPMSM [4]–[6]. At standstill or very low rotating speed, however, because the voltage from the back EMF, which has the position information, is proportional to the rotating speed, the signal is too weak to be used as position information. In the second group, rotor position is estimated from the characteristics of IPMSM: The spatial inductance distribution is determined by the rotor position because of the saliency of the magnetic path [7]–[18]. To extract the spatial inductance variation, the relationship between current and voltage is employed. To examine the current–voltage relationship, pulse width modulation (PWM) current ripple can be used [7]–[10]. By measuring the current variation according to the voltage vector variation in a PWM period, inductance can be calculated directly [7]–[9] or estimated with a nonlinear estimator [10]. However, these methods require the modification of the PWM switching pattern because the current variation in the conventional space vector PWM (SVPWM) is too small to be used for the calculation of the inductance. Moreover, additional devices to measure the phase currents in arbitrary time should be designed in control hardware, which might not be acceptable to many industry applications. Similarly, the intended discontinuous voltage signal injected method has been proposed [11]. In [11], a large voltage signal is injected for a very short time interval, and the current variation by the injected voltage signal is measured. From the measured current variation, the inductance and rotor position can be estimated. However, with this method, the rotor position information is discontinuously obtained, and the rotor position estimation and the overall control performance could be degraded.

Meanwhile, the continuous signal injection methods without PWM modification have been proposed, and the signal can be easily augmented into the conventional current control loop [12]–[18]. The continuous voltage signals into the IPMSM causes the current ripple, which reflects the rotor position. From the corresponding current ripple, the rotor position information can be extracted with a properly designed observer and/or a state filter. For each signal injection sensorless method, a

demodulation process should be incorporated to extract the rotor position-related value from the current ripple. These signal injection sensorless methods can be further classified into two categories according to where the signal is injected: the rotating voltage signal injection in the stationary reference frame [12], [18] and the pulsating voltage signal injection in the estimated rotor reference frame [13]–[17]. The rotating voltage signal methods inject the continuous signal spatially regardless of the rotor position, and the pulsating voltage signal methods inject the signal continuously pulsating on the estimated rotor reference frame and/or the stationary reference frame. These sensorless methods have unique characteristics according to the injected signal type. These characteristics of each sensorless method affect the rotor position detection performance. Many research results have been published regarding the relationships between sensorless methods and their performances [19], [20].

Even though each sensorless control method has unique characteristics according to the injection signal type and the demodulation process, in every sensorless method, the rotor position is obtained from the current response caused by the injected voltage signal. However, the measured currents contain not only current ripples by the intentionally injected voltage signal but also the extra one by the fundamental current control and/or by nonidealities in machine and inverter. To improve the position estimation accuracy, the only current ripple by the corresponding injected voltage should be extracted from the measured phase current.

Generally, the frequency of the injected voltage signal is determined between the current control bandwidth and the PWM switching frequency. As the frequency of the injected signal is getting higher, the dynamics of the sensorless control can be enhanced, and the interference between the injected signal and the fundamental components of the current control can be diminished. If the PWM switching frequency is near or above the audible frequency range, the acoustic noise by the injected signal can be remarkably reduced or totally eliminated. However, the synthesis of the injection voltage by PWM limits the injection frequency up to the PWM switching frequency ideally, and furthermore, the filter used in the demodulation process restricts the injection frequency.

In this paper, new sensorless methods for IPMSM drives are proposed to improve the sensorless control performance. This study focuses on the highest frequency signal injection to enhance the control bandwidth and reduce the acoustic noise simultaneously. By injecting the voltage signal whose frequency is the same as the PWM switching frequency, which is the theoretical maximum frequency in a drive system fed by a PWM inverter where the sampling of the current and updating PWM is done twice in a PWM switching period, the injected signal can be easily decoupled from the fundamental frequency, and the speed/torque control performance can be enhanced. Moreover, if the PWM switching frequency is near the audible range for most people, which is around 16 kHz, the acoustic noise due to the injected signal can be virtually eliminated, which may be a concern with the signal injection in some applications. The proposed signal injection methods are compatible to the stationary reference frame or to the estimated rotor reference frame.

II. BASIC PRINCIPLE OF HIGH-FREQUENCY VOLTAGE SIGNAL INJECTION SENSORLESS METHOD

A. Rotating Voltage Signal Injection in the Stationary Reference Frame

By exploiting the variation of the measured current, the spatial information related to the rotor position can be directly calculated easily. The voltage equation of IPMSM in the stationary d-/q-axis reference frame with currents and flux can be described as

$$\begin{bmatrix} v_{ds}^s \\ v_{qs}^s \end{bmatrix} = R_s \begin{bmatrix} i_{ds}^s \\ i_{qs}^s \end{bmatrix} + \frac{d}{dt} \begin{bmatrix} \lambda_{ds}^s \\ \lambda_{qs}^s \end{bmatrix} \tag{1}$$

where $[v_{ds}^s, v_{qs}^s]^{\mathrm{T}}$, $[i_{ds}^s, i_{qs}^s]^{\mathrm{T}}$, and $[\lambda_{ds}^s, \lambda_{qs}^s]^{\mathrm{T}}$ are the vectors of the stator voltage, current, and flux linkage in the stationary d-/q-axis reference frame, respectively. Physically, the flux linkages in the stationary reference frame in (1), $[\lambda_{ds}^s, \lambda_{qs}^s]^{\mathrm{T}}$, are function of the stator currents and the flux linkage of the rotor permanent magnet. Those flux linkages can be derived as

$$\begin{bmatrix} \lambda_{ds}^s \\ \lambda_{qs}^s \end{bmatrix} = \mathbf{L_S} \begin{bmatrix} i_{ds}^s \\ i_{qs}^s \end{bmatrix} + \lambda_f \begin{bmatrix} \cos \theta_r \\ \sin \theta_r \end{bmatrix} \tag{2}$$

where the inductance matrix, $\mathbf{L_S}$, is represented in terms of the d-/q-axis inductances, L_{ds} and L_{qs}, in the synchronous rotor reference frame and the rotor position, θ_r, as (3) and (4) and λ_f is the permanent-magnet flux linkage

$$\mathbf{L_S} = \begin{bmatrix} \Sigma L + \Delta L \cos 2\theta_r & \Delta L \sin 2\theta_r \\ \Delta L \sin 2\theta_r & \Sigma L - \Delta L \cos 2\theta_r \end{bmatrix} \tag{3}$$

$$\Sigma L = \frac{L_{ds} + L_{qs}}{2} \quad \Delta L = \frac{L_{ds} - L_{qs}}{2}. \tag{4}$$

Then, (1) can be represented in terms of motor parameters and the stator currents as

$$\begin{bmatrix} v_{ds}^s \\ v_{qs}^s \end{bmatrix} = R_s \begin{bmatrix} i_{ds}^s \\ i_{qs}^s \end{bmatrix} + \mathbf{L_S} \frac{d}{dt} \begin{bmatrix} i_{ds}^s \\ i_{qs}^s \end{bmatrix}$$
$$+ 2\Delta L \omega_r \begin{bmatrix} -\sin 2\theta_r & \cos 2\theta_r \\ \cos 2\theta_r & \sin 2\theta_r \end{bmatrix} \begin{bmatrix} i_{ds}^s \\ i_{qs}^s \end{bmatrix} + \omega_r \lambda_f \begin{bmatrix} -\sin \theta_r \\ \cos \theta_r \end{bmatrix} \tag{5}$$

where ω_r is the synchronous speed. Because of the saliency of IPMSM, the inductance matrix, $\mathbf{L_S}$, in (3) has the spatial information of the rotor position. From the inductance saliency, the rotor position can be obtained. Under the assumption that the high-frequency voltage signal is injected into the IPMSM and the rotating speed is almost zero, the voltage drop of the stator resistance and the back EMF voltages can be ignored. Therefore, the high-frequency impedance model of IPMSM can be simply expressed as

$$\begin{bmatrix} v_{dsh}^s \\ v_{qsh}^s \end{bmatrix} = L_S \frac{d}{dt} \begin{bmatrix} i_{dsh}^s \\ i_{qsh}^s \end{bmatrix} \tag{6}$$

where $[v_{dsh}^s, v_{qsh}^s]^{\mathrm{T}}$ and $[i_{dsh}^s, i_{qsh}^s]^{\mathrm{T}}$ are the injected high-frequency voltage vector and the corresponding current vector in the stationary reference frame, respectively. The spatial inductance variation in Fig. 1 shows the possibility to estimate the
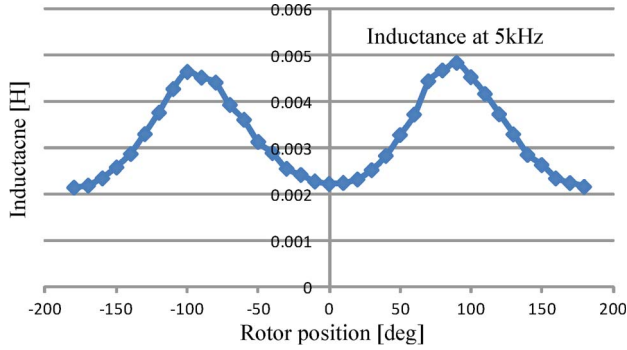
Fig. 1.   Inductance variation according to the rotor position at 5 kHz.

Fig. 2.   Block diagram of the heterodyning demodulation process in the rotating voltage vector injection method in the stationary reference frame.

rotor position from the inductance model in (6). According to the injected voltage signal, the current response can be derived from (6) as

$$\begin{bmatrix} i^s_{dsh} \\ i^s_{qsh} \end{bmatrix} = \int \mathbf{L_S}^{-1} \begin{bmatrix} v^s_{dsh} \\ v^s_{qsh} \end{bmatrix} dt. \tag{7}$$

If the voltage signal in (8) is injected to the stationary reference frame, the locus of the voltage vector would be a circle

$$v^s_{dqsh} = V_{inj} \begin{bmatrix} -\sin \omega_h t \\ \cos \omega_h t \end{bmatrix} \tag{8}$$

where V_{inj} and ω_h are the amplitude and frequency of the injection signal, respectively. According to this rotating voltage signal, the corresponding current response can be derived from (7) as

$$\begin{bmatrix} i^s_{dsh} \\ i^s_{qsh} \end{bmatrix} = \frac{V_{inj}}{\Sigma L^2 - \Delta L^2} \begin{bmatrix} \frac{\Sigma L}{\omega_h} \cos \omega_h t + \frac{\Delta L}{2\omega_r - \omega_h} \cos(2\theta_r - \omega_h t) \\ \frac{\Sigma L}{\omega_h} \sin \omega_h t + \frac{\Delta L}{2\omega_r - \omega_h} \sin(2\theta_r - \omega_h t) \end{bmatrix}. \tag{9}$$

From the current response, (9), the rotor position information can be extracted through a kind of signal processing called as the demodulation process. In [12], the heterodyning demodulation process has been proposed as shown in Fig. 2. In this demodulation process, the current responses in (9) are multiplied with a sinusoidal function whose frequency is identical to the injection frequency. After low-pass filtering, the final result of the demodulation process, e_f, in Fig. 2 can be derived as the following:

$$\varepsilon_f \approx \frac{-V_{inj}}{\Sigma L^2 - \Delta L^2} \frac{\Delta L}{\omega_h} 2(\theta_r - \hat{\theta}_r) \tag{10}$$

where the signal injection frequency, ω_h, is assumed to be large enough compared to the rotating speed, ω_r, $(\omega_h \gg \omega_r)$ and the rotor position error between the real position and the estimated position is reasonably small. The result of the process, e_f, can be used as a corrective error input to the Luenberger style observer or state filter as shown in Fig. 2 [13]. In this paper, some new sensorless control methods are proposed. These methods are focused on the realization to extract the position error with switching frequency signal injection. Therefore, the Luenberger style observer or state filter in Fig. 2 should be also
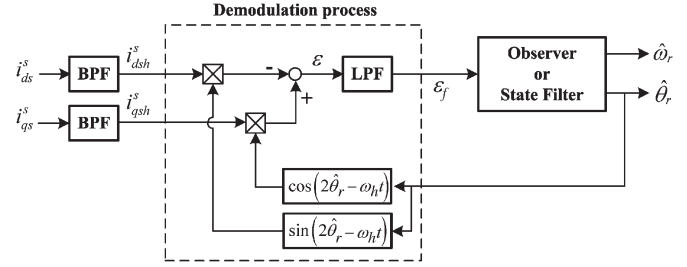
accompanied by the proposed methods. By driving e_f to zero, the observer or state filter enforces the estimated rotor position to follow the actual rotor position.

B. Pulsating Voltage Signal Injection in the Estimated Rotor Reference Frame

As the rotor position information is derived from the inductance matrix in the stationary reference frame, the rotor position-related information can be also extracted from the current–voltage relationship in the estimated rotor reference frame. The voltage equation in the rotor reference frame can be described as

$$\begin{bmatrix} v^r_{ds} \\ v^r_{qs} \end{bmatrix} = R_s \begin{bmatrix} i^r_{ds} \\ i^r_{qs} \end{bmatrix} + \begin{bmatrix} L_{ds} & 0 \\ 0 & L_{qs} \end{bmatrix} \frac{d}{dt} \begin{bmatrix} i^r_{ds} \\ i^r_{qs} \end{bmatrix}$$
$$+ \omega_r \begin{bmatrix} 0 & -L_{qs} \\ L_{ds} & 0 \end{bmatrix} \begin{bmatrix} i^r_{ds} \\ i^r_{qs} \end{bmatrix} + \omega_r \lambda_f \begin{bmatrix} 0 \\ 1 \end{bmatrix} \tag{11}$$

where $[v^r_{ds}, v^r_{qs}]^{\mathrm{T}}$ and $[i^r_{ds}, i^r_{qs}]^{\mathrm{T}}$ are the vectors of the stator voltage and current in the rotor reference frame, respectively. Supposing that the high-frequency voltage signal is injected into the IPMSM, the high-frequency impedance model in the rotor reference frame can be simply described as

$$\begin{bmatrix} v^r_{dsh} \\ v^r_{qsh} \end{bmatrix} = \begin{bmatrix} L_{ds} & 0 \\ 0 & L_{qs} \end{bmatrix} \frac{d}{dt} \begin{bmatrix} i^r_{dsh} \\ i^r_{qsh} \end{bmatrix} \tag{12}$$

where $[v^r_{dsh}, v^r_{qsh}]^{\mathrm{T}}$ and $[i^r_{dsh}, i^r_{qsh}]^{\mathrm{T}}$ are the vector of the injection frequency voltage component and current component in the rotor reference frame, respectively. According to the injection voltage signal, the current response can be derived from (12) as

$$\begin{bmatrix} i^r_{dsh} \\ i^r_{qsh} \end{bmatrix} = \int \begin{bmatrix} L_{ds} & 0 \\ 0 & L_{qs} \end{bmatrix}^{-1} \begin{bmatrix} v^r_{dsh} \\ v^r_{qsh} \end{bmatrix} dt. \tag{13}$$

Fig. 3 shows the relationship in the reference axes. The position error $\tilde{\theta}_r$ between the real position θ_r and the estimated position $\hat{\theta}_r$ can be described as

$$\tilde{\theta}_r = \theta_r - \hat{\theta}_r. \tag{14}$$

When the pulsating voltage signal is injected into the d-axis in the rotor reference frame, the corresponding current response
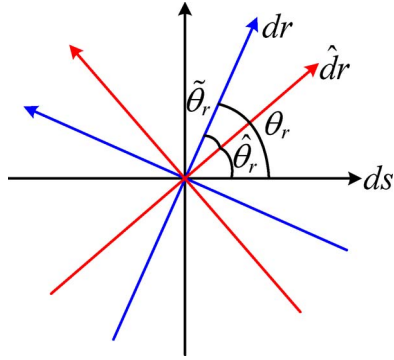
Fig. 3. Relationship between reference axes. (Black) Stationary reference frame, (blue) real rotor reference frame, and (red) estimated rotor reference frame.

leads to estimate the rotor position. The pulsating voltage signal in the rotor reference frame can be described as

$$\begin{bmatrix} v_{dsh}^r \\ v_{qsh}^r \end{bmatrix} = V_{inj} \begin{bmatrix} \cos \omega_h t \\ 0 \end{bmatrix}. \qquad (15)$$

Then, the corresponding current response can be derived as (16) from (13)

$$\begin{bmatrix} i_{dsh}^r \\ i_{qsh}^r \end{bmatrix} = \frac{V_{inj}}{L_{ds}\omega_h} \begin{bmatrix} \sin \omega_h t \\ 0 \end{bmatrix}. \qquad (16)$$

If the saturation effect is neglected and the pulsating voltage signal is injected into the exact d-axis rotor reference frame, the q-axis current ripple due to the injected voltage does not happen [20]. However, because the real rotor position is not available, the injected voltage signal actually differs from the one injected at the real d-axis, (15). The injection voltage in the estimated rotor reference frame can be rewritten with consideration of the estimated rotor position error as

$$V_{dqsh}^{\hat{r}} = V_{inj} \begin{bmatrix} \cos \omega_h t \\ 0 \end{bmatrix}. \qquad (17)$$

Considering the position error, the actual injection voltage signal into the real rotor reference frame can be described as

$$V_{dqsh}^r = T(\tilde{\theta}_r) V_{dqsh}^{\hat{r}} = V_{inj} \begin{bmatrix} \cos \tilde{\theta}_r \cos \omega_h t \\ -\sin \tilde{\theta}_r \cos \omega_h t \end{bmatrix} \qquad (18)$$

where $T(\tilde{\theta}_r)$ stands for the transformation from the estimated rotor reference frame to the real rotor reference frame. Then, the corresponding current response in the estimated rotor reference frame can be deduced as

$$\begin{aligned} \begin{bmatrix} i_{dsh}^{\hat{r}} \\ i_{qsh}^{\hat{r}} \end{bmatrix} &= T(\tilde{\theta}_r)^{-1} \begin{bmatrix} i_{dsh}^r \\ i_{qsh}^r \end{bmatrix} \\ &= \frac{V_{inj}}{\omega_h} \begin{bmatrix} \left(\frac{\cos^2 \tilde{\theta}_r}{L_{ds}} + \frac{\sin^2 \tilde{\theta}_r}{L_{qs}} \right) \sin \omega_h t \\ \frac{1}{2} \left(\frac{-\Delta L}{L_{ds}L_{qs}} \right) \sin 2\tilde{\theta}_r \sin \omega_h t \end{bmatrix}. \end{aligned} \qquad (19)$$

It can be seen from (19) that the rotor position error is placed in the estimated q-axis current response. Using the heterodyning demodulation process in Fig. 4, the position error can be extracted from the q-axis current response. The final result of
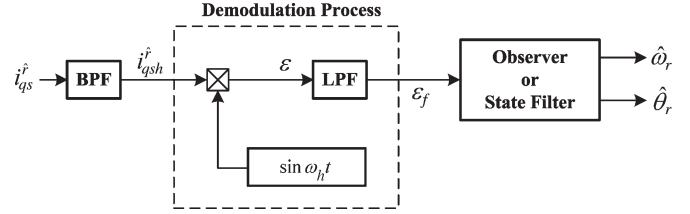

Fig. 4. Block diagram of the heterodyning demodulation process.

the demodulation process from the method in Fig. 4, e_f, can be derived as

$$\varepsilon_f \approx \frac{1}{2} \frac{V_{inj}}{\omega_h} \left(\frac{-\Delta L}{L_{ds}L_{qs}} \right) (\theta_r - \hat{\theta}_r) \qquad (20)$$

under the assumption that the error between the real rotor position and the estimated one is small. In the same manner as the rotating signal injection method in the previous section, the demodulation process result, e_f, can be used as a corrective error input to the observer or state filter in Fig. 4.

III. PROPOSED PWM SWITCHING FREQUENCY SIGNAL INJECTION SENSORLESS METHODS

By increasing the injection frequency, the performance of the sensorless system such as the system control bandwidth has been enhanced [15], [16]. In these papers, the injection frequency was increased up to a half of the PWM switching frequency due to the discrete-type filter implementation and delay issues in the demodulation process [16]. In [8] and [9], the PWM switching frequency signal injection has been tried already. However, the PWM switching patterns have to be modified, the current should be measured at the specified time point in the switching period, and the time point is varying. In this paper, the PWM switching frequency voltage signal injection methods are proposed. The proposed methods have neither PWM modification nor current measurement problem. The high-frequency discrete filter is not used in the demodulation process, and the advantages using high-frequency signal injection are fully exploited. These methods can be implemented in both the stationary reference frame and the estimated rotor reference frame.

A. PWM Switching Frequency Signal Injection in the Stationary Reference Frame

The voltage equation can be rewritten as (21), where the derivative of current is expressed in discrete form as current variation ($\Delta i_{ds}^s, \Delta i_{qs}^s$) in a sampling interval ΔT

$$\begin{aligned} \begin{bmatrix} v_{ds}^s \\ v_{qs}^s \end{bmatrix} &= R_s \begin{bmatrix} i_{ds}^s \\ i_{qs}^s \end{bmatrix} + \omega_r \lambda_f \begin{bmatrix} -\sin \theta_r \\ \cos \theta_r \end{bmatrix} + L_S \frac{1}{\Delta T} \begin{bmatrix} \Delta i_{ds}^s \\ \Delta i_{qs}^s \end{bmatrix} \\ &\quad + 2\Delta L \omega_r \begin{bmatrix} -\sin 2\theta_r & \cos 2\theta_r \\ \cos 2\theta_r & \sin 2\theta_r \end{bmatrix} \begin{bmatrix} i_{ds}^s \\ i_{qs}^s \end{bmatrix}. \end{aligned} \qquad (21)$$

In (21), the rotor position information is on the inductance matrix, $\mathbf{L_S}$. If the inductance matrix can be extracted from (21), the rotor position can be estimated in real time. In [8], the inductance matrix was calculated with the high-frequency impedance
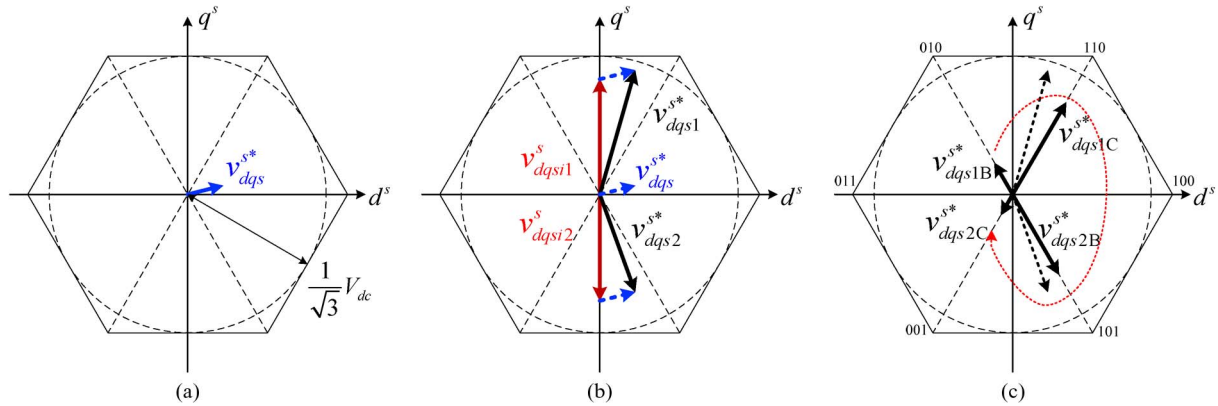
Fig. 5.   Modified voltage references at stationary voltage plane. (a) Fundamental voltage reference, (b) injection voltage, and (c) split voltage reference.

model as (6). Because the inductance matrix, $\mathbf{L_S}$ is a 2 by 2 matrix, two independent voltage vectors and current vectors have to be used in the calculation. To improve the accuracy in the inductance calculation, the voltage difference method [18] is adapted in the demodulation process. The voltage vector used in the calculation is not the one voltage vector but the voltage difference between two successive voltage vectors. For example, the difference between two independent voltage vectors, (v_{ds1}^s, v_{qs1}^s) and (v_{ds2}^s, v_{qs2}^s), can be derived by the multiplication inductance matrix, $\mathbf{L_S}$, and current difference as (22) where Δi_{dqs1}^s and Δi_{dqs2}^s mean the current variation in each voltage vector, v_{dqs1}^s and v_{dqs2}^s, respectively. The inductance matrix can be represented as (23) in terms of two voltage difference vectors. From (23), the rotor position information can be directly calculated as (24). In the calculation of the matrix inversion in (23), the determinant of the matrix is required. Since it is eliminated as shown in (24), eight multiplications and four additions are simply needed in the calculations

$$\begin{bmatrix} v_{ds21}^s \\ v_{qs21}^s \end{bmatrix} = \begin{bmatrix} v_{ds2}^s - v_{ds1}^s \\ v_{qs2}^s - v_{qs1}^s \end{bmatrix} = L_S \frac{1}{\Delta T} \begin{bmatrix} \Delta i_{ds2}^s - \Delta i_{ds1}^s \\ \Delta i_{qs2}^s - \Delta i_{qs1}^s \end{bmatrix}$$

$$= L_S \frac{1}{\Delta T} \begin{bmatrix} \Delta i_{ds21}^s \\ \Delta i_{qs21}^s \end{bmatrix} \tag{22}$$

$$L_S = \Delta T \begin{bmatrix} v_{ds32}^s & v_{ds21}^s \\ v_{qs32}^s & v_{qs21}^s \end{bmatrix} \begin{bmatrix} \Delta i_{ds32}^s & \Delta i_{ds21}^s \\ \Delta i_{qs32}^s & \Delta i_{qs21}^s \end{bmatrix}^{-1}$$

$$= \begin{bmatrix} L_{11} & L_{12} \\ L_{21} & L_{22} \end{bmatrix} \tag{23}$$

$$2\hat{\theta}_{rCal} = \tan^{-1} \left(\frac{L_{12} + L_{21}}{L_{11} - L_{22}} \right). \tag{24}$$

To get two independent voltage vectors in one PWM switching period, one voltage vector in a half PWM switching frequency can be split into the two voltage vectors as shown in Fig. 5. The fundamental voltage reference in Fig. 5(a) means the output voltage reference of the current controller. With the injected voltage, v_{dqsi1}^s and v_{dqsi2}^s, the voltage references are modified as v_{dqs1}^{s*} and v_{dqs2}^{s*} as shown in Fig. 5(b). The modified voltage references v_{dqs1}^{s*} can be split into v_{dqs1B}^{s*} and v_{dqs1C}^{s*}, and v_{dqs2}^{s*} can be split into v_{dqs2B}^{s*} and v_{dqs2C}^{s*} in a PWM period as shown in Fig. 5(c). Therefore, four voltage vectors which induce the additional current ripple can be obtained in every
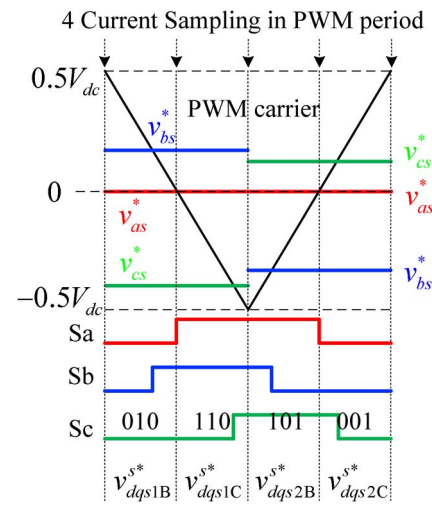

Fig. 6.   PWM sequence with PWM switching voltage injection.

PWM switching period. A fluctuating voltage signal at the fixed axis is injected where positive voltage and negative voltage are added in half of the switching period, respectively, as shown in Fig. 5(c).

The magnitude of the injected voltage is determined according to the sensorless performance. If the magnitude of the injected voltage is large, the current ripple is increased, and the rotor position error can be extracted clearly. However, this large current ripple causes additional core loss and acoustic noises. If the magnitude of the injected voltage is small, the core loss is decreased. However, the rotor position error cannot be clearly extracted.

To calculate the inductance matrix, $\mathbf{L_S}$, the corresponding current according to each voltage vector should be measured. In Fig. 6, the sequence related to the voltage vectors and corresponding current sampling time points are displayed together with the triangular carrier wave. From the figure, it can be seen that the sampling of the current is executed four times in a switching period. The PWM sequence can be easily implemented using the carrier-based offset voltage PWM concept in [21].

To use the four voltage vectors and the corresponding current values, the split voltage vectors $(v_{dqs1B}^{s*}, v_{dqs1C}^{s*})$ and $(v_{dqs2B}^{s*}, v_{dqs2C}^{s*})$ have to change from v_{dqs1B}^{s*} to v_{dqs1C}^{s*} and
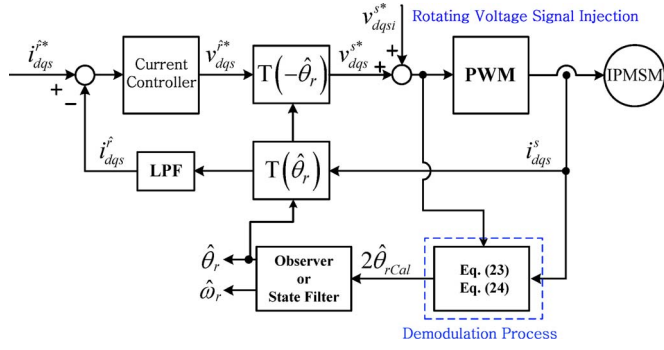
Fig. 7. Block diagram of the proposed rotating voltage signal injection method at PWM switching frequency.

TABLE I
PARAMETERS OF IPMSM AND DRIVES SYSTEM

	Item	Quantity
IPMSM Parameter	Rated Power	11kW
	Rated Speed	1750r/min
	Rated current	39.5Arms
	Stator Resistance	0.14Ω
	Nominal Inductance	L_{ds}: 3.4mH / L_{qs}: 4.3mH
	PM Flux linkage	λ_f: 0.253V·s
System Parameter	DC-link Voltage	310V
	PWM Switching Freq.	5kHz
	Current Sampling Freq.	10kHz
	Current Control Bandwidth	300Hz
	Speed Control Bandwidth	25Hz

from v^{s*}_{dqs2B} to v^{s*}_{dqs2C} at the center of the half PWM switching period as shown in Fig. 6. To extract the position information, the voltage and current vectors which are used in the calculation are derived as in (22). The inductance matrix can be determined as in (23).

The overall block diagram of the proposed rotating voltage injection sensorless method in the stationary reference frame is shown in Fig. 7. In the current feedback loop, the first-order low-pass filter (LPF) still exists. However, because the frequency of the current ripple is the same as the PWM switching one, the LPF is very weak, and the cutoff frequency can be increased up to a half of the PWM switching frequency. Where the PWM switching frequency is 5 kHz, the bandwidth of the LPF is 2.5 kHz. To obtain four sampling instances within one PWM period, samplings at zero-crossing points are added in the conventional peak and valley samplings. Here, it can be implemented without any additional hardware.

In the proposed methods, current sampling is very important. Since the sampled currents are used for position calculation, the sampling errors cause critical problems in rotor position estimation. There are two major causes in the sampling errors: sampling delay in sampling process from current sensors to the A/D converter, and switching transients. The sampling delay can be compensated by delaying the sampling instance, and the switching transients such as oscillation should be avoided properly. In the proposed methods, the instances of zero cross samplings are on the edge of the voltage vector just before voltage vector change. Therefore, the current oscillation can be avoided naturally.

To verify the proposed sensorless method, as a test setup, an 11-kW IPMSM drive system coupled to a load machine was used. IPMSM parameters and the drive system parameters are listed in Table I. These parameters are also used for the simulation in the previous figures. The PWM switching frequency is 5 kHz, and the current sampling frequency for current control is 10 kHz. For sensorless operation, currents are measured four times in one PWM period. The current signal due to the injected voltage signal is shown in the lower figure of Fig. 8(a). In Fig. 8(b), the speed control performance under speed reference variation from −200 to 200 r/min with load is demonstrated. To show the current regulation performance, the results of a current regulation at standstill according to a 300-Hz sinusoidal current reference with a positive offset were displayed in Fig. 8(c).

In this experiment, the load machine was controlled in zero speed control mode. Because the proposed method considers not only the injected high-frequency voltages but also the total voltages, including the output voltage of the current controller, the directly calculated position error can be reduced. Moreover, the injection frequency is the PWM switching one, 5 kHz, and the 300-Hz current reference does not degrade the rotor position tracking performance at all, even with this relatively high current regulation bandwidth.

B. Pulsating Voltage Signal Injection in the Estimated Rotor Reference Frame

Through the same way as described in the previous section, the current ripple due to the pulsating voltage signal in the estimated rotor reference frame can be calculated by using the measured current difference. Equation (25) describes the voltage equation of IPMSM in the d-/q-axis rotor reference frame

$$\begin{bmatrix} v^r_{ds} \\ v^r_{qs} \end{bmatrix} = R_s \begin{bmatrix} i^r_{ds} \\ i^r_{qs} \end{bmatrix} + \begin{bmatrix} L_{ds} & 0 \\ 0 & L_{qs} \end{bmatrix} \frac{1}{\Delta T} \begin{bmatrix} \Delta i^s_{ds} \\ \Delta i^s_{qs} \end{bmatrix}$$
$$+ \omega_r \left(\begin{bmatrix} 0 & -L_{qs} \\ L_{qs} & 0 \end{bmatrix} \begin{bmatrix} i^s_{ds} \\ i^s_{qs} \end{bmatrix} + \begin{bmatrix} 0 \\ \lambda_f \end{bmatrix} \right). \quad (25)$$

To estimate the rotor position, the pulsating voltage signals $v^{\hat r}_{dsi} v^{\hat r}_{qsi}$ of which the frequency is the PWM switching one can be injected as shown in Fig. 9. Only at the d-axis in the estimated rotor reference frame is the square wave signal injected, and the currents are measured two times for every PWM period. This high-frequency voltage signal causes the same frequency current ripples based on the high-frequency inductance model of IPMSM as

$$\begin{bmatrix} v^r_{dsh} \\ v^r_{qsh} \end{bmatrix} = \begin{bmatrix} L_{ds} & 0 \\ 0 & L_{qs} \end{bmatrix} \frac{1}{\Delta T} \begin{bmatrix} \Delta i^r_{dsh} \\ \Delta i^r_{qsh} \end{bmatrix}. \quad (26)$$

Because the high-frequency signal is injected on the estimated rotor reference frame, the voltage signal in the real rotor reference frame includes the following position error:

$$V^r_{dqsh} = T(\tilde\theta_r)V^{\hat r}_{dqsh} = \pm V_{inj} \begin{bmatrix} \cos\tilde\theta_r \\ -\sin\tilde\theta_r \end{bmatrix}. \quad (27)$$
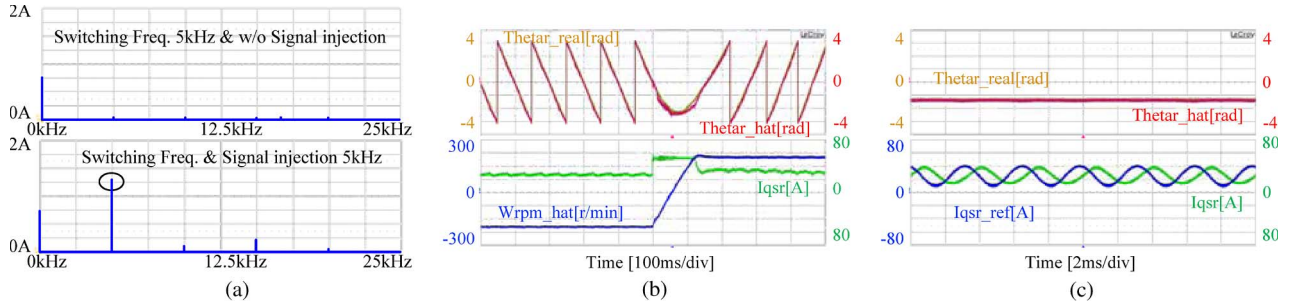
Fig. 8.   Rotating signal injection sensorless control performance (injection frequency: 5 kHz). (a) Phase current FFT results, (b) speed control from −200 to 200 r/min, and (c) current control (300-Hz reference).
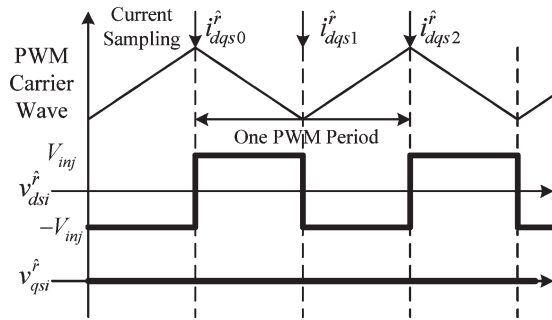

Fig. 9.   Pulsating injection voltage signal in the estimated rotor reference frame. In a PWM period, three successively measured currents are used to estimate the rotor position.

By the voltage signal in (27), the current ripple in (28) can be derived from (26). In the same manner, the currents can be only measured in the estimated rotor reference frame as

$$\begin{bmatrix} \Delta i_{dsh}^{r} \\ \Delta i_{qsh}^{r} \end{bmatrix} = \pm \Delta T \cdot V_{inj} \begin{bmatrix} \frac{1}{L_{ds}} \cos \tilde{\theta}_r \\ \frac{-1}{L_{qs}} \sin \tilde{\theta}_r \end{bmatrix} \quad (28)$$

$$\begin{bmatrix} \Delta i_{dsh}^{\hat{r}} \\ \Delta i_{qsh}^{\hat{r}} \end{bmatrix} = T_{\tilde{\theta}_r}^{-1} \begin{bmatrix} \Delta i_{dsh}^{r} \\ \Delta i_{qsh}^{r} \end{bmatrix}$$

$$= \pm \Delta T \cdot V_{inj} \begin{bmatrix} \frac{\cos^2 \tilde{\theta}_r}{L_{ds}} + \frac{\sin^2 \tilde{\theta}_r}{L_{qs}} \\ \frac{1}{2} \left(\frac{1}{L_{ds}} - \frac{1}{L_{qs}} \right) \sin 2\tilde{\theta}_r \end{bmatrix}. \quad (29)$$

Theoretically, the rotor position error information is dependent on the q-axis current ripple in the estimated rotor reference frame as (29). Therefore, the estimated q-axis current ripple can be used as the rotor position error for sensorless control.

When the fundamental current controller and the injected pulsating voltages are determined as shown in Fig. 9, the current ripple due to only the injected voltage signal can be calculated easily. Fig. 10 shows the voltage references and the corresponding current responses. The d-/q-axis voltage references (30) from the current control loop consist of two components: fundamental voltage as (31) and current control voltage as (32). The fundamental voltages in (31) mean the resistance voltage drop and back EMF voltages. Moreover, the current control voltages in (32) mean the portion which causes the current variation in the voltage reference of the current control loop

$$v_{ds}^{\hat{r}} = v_{dsf}^{\hat{r}} + v_{dsc}^{\hat{r}} = R_s i_{ds}^{\hat{r}} - \omega_r L_{qs} i_{qs}^{\hat{r}} + L_{ds} \frac{d i_{ds}^{\hat{r}}}{dt}$$

$$v_{qs}^{\hat{r}} = v_{qsf}^{\hat{r}} + v_{qsc}^{\hat{r}} = R_s i_{qs}^{\hat{r}} + \omega_r L_{ds} i_{ds}^{\hat{r}} + \omega_r \lambda_f + L_{qs} \frac{d i_{qs}^{\hat{r}}}{dt} \quad (30)$$
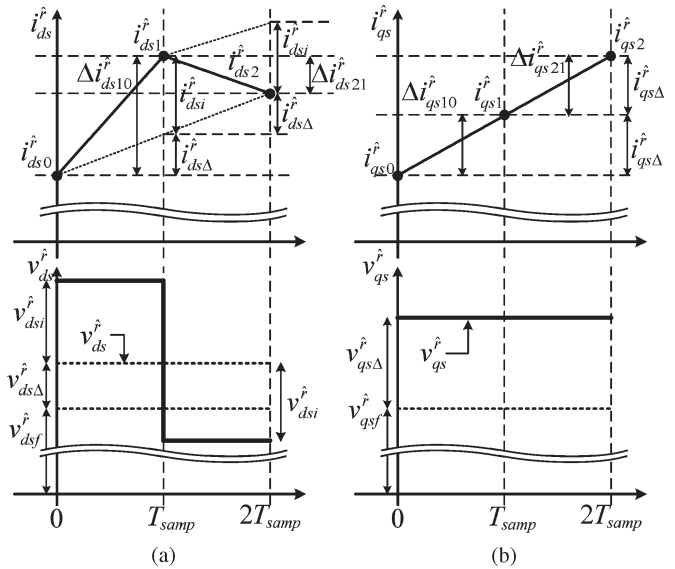

Fig. 10.   Estimated rotor reference frame voltage signal injection. (a) d-axis voltage reference and injected signal in a PWM period and the corresponding current response. (b) q-axis voltage reference and the corresponding current response.

$$v_{dsf}^{\hat{r}} = R_s i_{ds}^{\hat{r}} - \omega_r L_{qs} i_{qs}^{\hat{r}}$$

$$v_{qsf}^{\hat{r}} = R_s i_{qs}^{\hat{r}} + \omega_r L_{ds} i_{ds}^{\hat{r}} + \omega_r \lambda_f \quad (31)$$

$$v_{dsc}^{\hat{r}} = L_{ds} \frac{d i_{ds}^{\hat{r}}}{dt} \qquad v_{qsc}^{\hat{r}} = L_{qs} \frac{d i_{qs}^{\hat{r}}}{dt}. \quad (32)$$

However, when the voltage signals are added, the current ripples occur by two voltages: the current control voltage and the injection voltage. For the rotor position estimation, the current ripple due to only the injected voltage signal should be extracted from the current ripples. Fig. 10 shows the voltage references and the corresponding current ripples. For a PWM period, the estimated d-/q-axis current variations by the current control voltage are $2i_{ds\Delta}^{\hat{r}}$ and $2i_{qs\Delta}^{\hat{r}}$, respectively, and the current ripples by the injection signal are $i_{dsi}^{\hat{r}}$ and $i_{qsi}^{\hat{r}}$. The current ripples due to only the injection signal can be obtained from the three successively sampled currents. The current ripple in the first half PWM period consists of the fundamental current ripple, $i_{dqs\Delta}^{\hat{r}}$, and injection signal current ripple, $i_{dqsi}^{\hat{r}}$ as (33). In the second half PWM period, the current ripples can be represented as (34). Therefore, the current ripple due to the
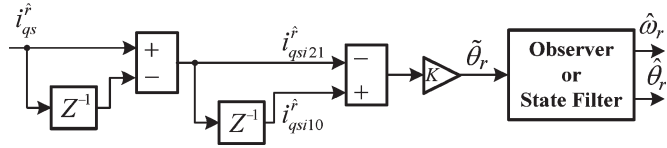
Fig. 11. Proposed demodulation process with high-frequency signal injection in the estimated rotor reference frame.
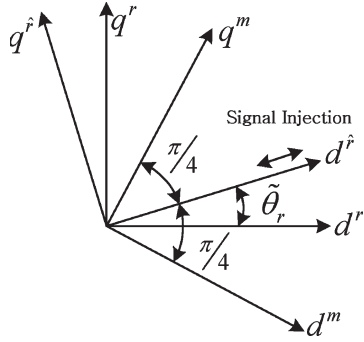

Fig. 12. Real axis, estimated axis, and measurement axis in the rotor reference frame [14], [22].

Fig. 13. Block diagram of the proposed pulsating voltage signal injection method with the switching frequency signal injection.

only injection signal can be obtained as the difference between current ripples in two half PWM periods as (35)

$$\Delta i_{ds10}^{\hat{r}} = i_{ds1}^{\hat{r}} - i_{ds0}^{\hat{r}} = i_{ds\Delta}^{\hat{r}} + i_{dsi}^{\hat{r}}$$

$$\Delta i_{qs10}^{\hat{r}} = i_{qs1}^{\hat{r}} - i_{qs0}^{\hat{r}} = i_{qs\Delta}^{\hat{r}} + i_{qsi}^{\hat{r}} \tag{33}$$

$$\Delta i_{ds21}^{\hat{r}} = i_{ds2}^{\hat{r}} - i_{ds1}^{\hat{r}} = i_{ds\Delta}^{\hat{r}} - i_{dsi}^{\hat{r}}$$

$$\Delta i_{qs21}^{\hat{r}} = i_{qs2}^{\hat{r}} - i_{qs1}^{\hat{r}} = i_{qs\Delta}^{\hat{r}} - i_{qsi}^{\hat{r}} \tag{34}$$

$$\Delta i_{ds10}^{\hat{r}} - \Delta i_{ds21}^{\hat{r}} = 2i_{dsi}^{\hat{r}}$$

$$\Delta i_{qs10}^{\hat{r}} - \Delta i_{qs21}^{\hat{r}} = 2i_{qsi}^{\hat{r}} \tag{35}$$

$$\begin{bmatrix} i_{dsi}^{\hat{r}} \\ i_{qsi}^{\hat{r}} \end{bmatrix} = \begin{bmatrix} \Delta i_{ds10}^{\hat{r}} - \Delta i_{ds21}^{\hat{r}} \\ \Delta i_{qs10}^{\hat{r}} - \Delta i_{qs21}^{\hat{r}} \end{bmatrix}$$

$$= 2\Delta T \cdot V_{inj} \begin{bmatrix} \frac{\cos^2 \tilde{\theta}_r}{L_{ds}} + \frac{\sin^2 \tilde{\theta}_r}{L_{qs}} \\ \frac{1}{2} \left(\frac{1}{L_{ds}} - \frac{1}{L_{qs}} \right) \sin 2\tilde{\theta}_r \end{bmatrix}. \tag{36}$$

From (29), the calculated current ripple can be rewritten as (36). In this case, the demodulation process can be substituted by the only current ripple calculation given by (33)–(35) with neither LPF nor bandpass filter. Fig. 11 shows the block diagram for rotor position estimation. The position error is proportional to the difference of two current ripples in the estimated q-axis with the constant K as

$$\tilde{\theta}_r = K i_{qsi}^{\hat{r}} = K \left(\Delta i_{qs10}^{\hat{r}} - \Delta i_{qs21}^{\hat{r}} \right) \tag{37}$$

$$K = \frac{L_{ds} L_{qs}}{2(L_{qs} - L_{ds})\Delta T \cdot V_{inj}}. \tag{38}$$

The rotor position error between the real rotor position and the estimated rotor position can be also obtained by other demodulation process in [14] and [22]. To extract the position
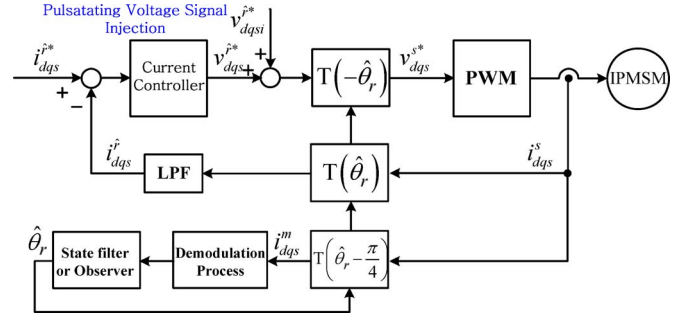
error, $\tilde{\theta}_r$, from the current ripple, the orthogonal measurement axes, the d^m- and q^m-axes shown in Fig. 12, have been used. The difference between the d^m-axis current ripple and the q^m-axis one in (39) is proportional to the rotor position error between the real rotor position and the estimated rotor position as (40).

With a state filter or an observer, the rotor position can be estimated through (40). The entire control block diagram of the proposed pulsating signal injection sensorless method with the switching frequency signal injection is shown in Fig. 13

$$\begin{bmatrix} i_{dsi}^m \\ i_{qsi}^m \end{bmatrix} = T_{-\frac{\pi}{4}} \begin{bmatrix} i_{dsi}^{\hat{r}} \\ i_{qsi}^{\hat{r}} \end{bmatrix}$$

$$= \pm \frac{\Delta T \cdot V_{inj}}{\sqrt{2}}$$

$$\times \begin{bmatrix} \frac{\cos^2 \tilde{\theta}_r}{L_{ds}} + \frac{\sin^2 \tilde{\theta}_r}{L_{qs}} - \frac{1}{2} \left(\frac{1}{L_{ds}} - \frac{1}{L_{qs}} \right) \sin 2\tilde{\theta}_r \\ \frac{\cos^2 \tilde{\theta}_r}{L_{ds}} + \frac{\sin^2 \tilde{\theta}_r}{L_{qs}} + \frac{1}{2} \left(\frac{1}{L_{ds}} - \frac{1}{L_{qs}} \right) \sin 2\tilde{\theta}_r \end{bmatrix} \tag{39}$$

$$\tilde{\theta}_r = K \left(\left| i_{qsi}^m \right| - \left| i_{dsi}^m \right| \right). \tag{40}$$

To verify the proposed pulsating signal injection sensorless method, the same test setup of the case of the signal injection to the stationary reference frame was used. The PWM switching frequency is 5 kHz, and the current sampling frequency is 10 kHz. In Fig. 14(a), the speed control performance under the speed reference change from −200 to 200 r/min with load is shown, and the current regulation performance at standstill was demonstrated in Fig. 14(b) and (c). The results show lower ripples than the results in Fig. 8. The difference may come from the multiple saliency of the motor because the rotating signal injection is rather sensitive to the multiple saliency of the motor [23].

Even though the rotor position can be estimated exactly in various operating condition, the injected signals produce non-negligible acoustic noises. This noise problem tends to restrict the application of the signal injection sensorless control. There are two ways to reduce these acoustic noises: minimizing the magnitude of the injected signal and increasing the frequency of the injected signal near or above the audible frequency range. The former can be a fundamental solution. However, the magnitude of the injected signal should be determined by the accuracy and resolution of the current measurement. In most cases, they are decided by the hardware setup of the inverter,
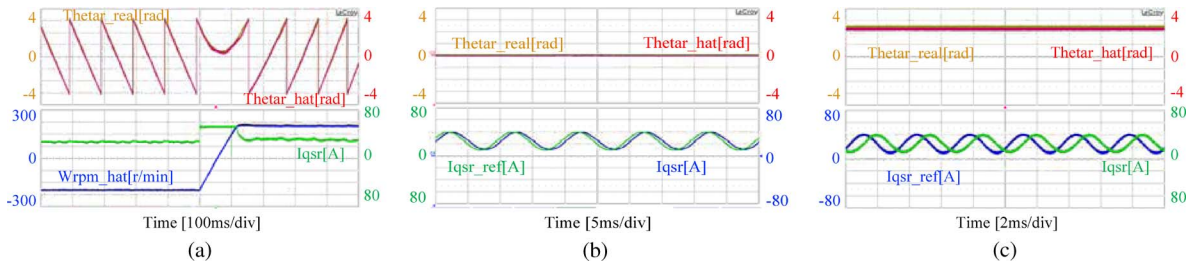
Fig. 14. Pulsating signal injection sensorless control performance (injection frequency: 5 kHz). (a) Speed control from −200 to 200 r/min, (b) current control (100-Hz reference), and (c) current control (300-Hz reference).
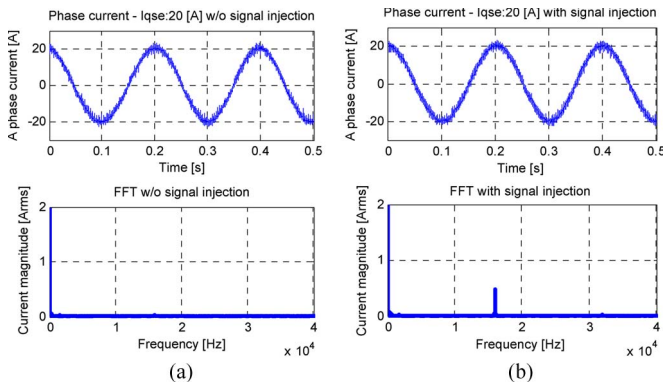

Fig. 15. Phase currents and their FFT with 30% load condition (16-kHz signal injection). (a) Without signal injection. (b) With signal injection.

Fig. 16. Step current response (16-kHz signal injection). (a) 20-A step reference. (b) 50-A step reference.

and the latter may be used for the reduction of the acoustic noise. However, the maximum injected frequency is limited by the PWM switching frequency.

Owing to the proposed methods, the frequency of the injected signal can be increased up to the switching frequency itself. If the PMW switching frequency is set as 16 kHz, which is almost the boundary frequency of the human audible frequency range, the acoustic noise can be virtually eliminated. The same test setup of the previous experiments, except for the PWM switching frequency, was used to verify the elimination of the acoustic noise. The PWM switching frequency is 16 kHz, and the switch devices are conventional insulated gate bipolar transistor modules. The maximum switching frequency is guaranteed up to 20 kHz by the manufacturer of the module. Fig. 15 shows the phase currents in 30% load condition. In Fig. 15(a), the phase currents and their fast Fourier transform (FFT) result without signal injection are presented. With a 16-kHz signal injection, the current component at 16 kHz is shown in Fig. 15(b). The magnitude of the current at 16 kHz was 0.5 Arms, which could be adjusted by the magnitude of the injected signal. The acoustic noise caused by the injected signal disappeared.

Fig. 16 shows the current control performance. The bandwidth of the current control loop was 700 Hz, and the rated current is 54 A. The q-axis current reference was varied from 0 A to 20 A and 50 A, respectively. As shown in Fig. 16, the position estimation error was maintained within ±0.25 rad, even if the q-axis current varied rapidly. In the steady state, the position error varied according to the stator current. This error is caused by the flux saturation [20].
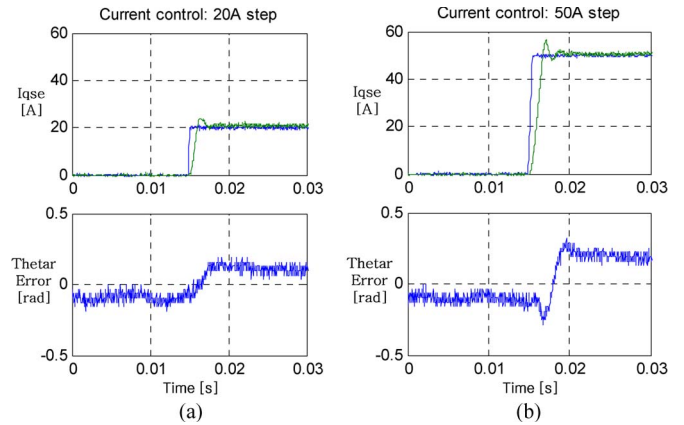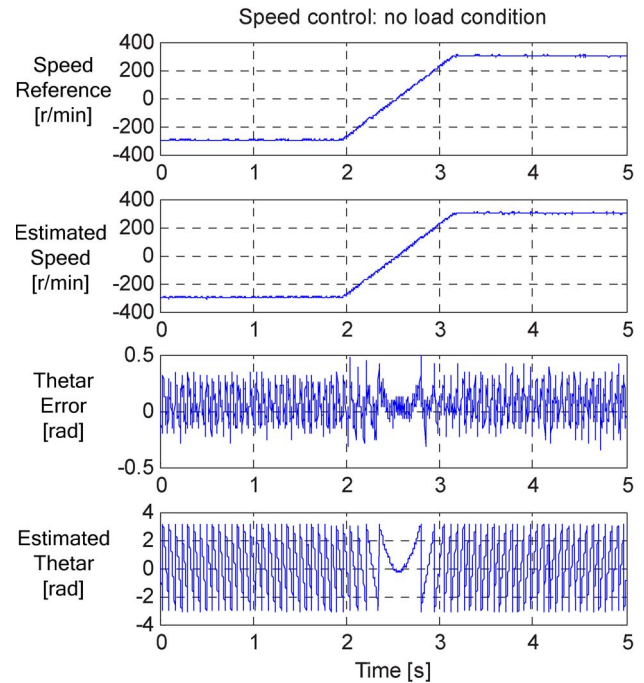

Fig. 17. Speed control from −300 to 300 r/min without load. Speed reference, estimated speed, position error, and estimated rotor position.

In Figs. 17–19, the speed control performances were demonstrated. In the no-load condition, the speed reference was changed from −300 to 300 r/min slowly, as shown in Fig. 17,
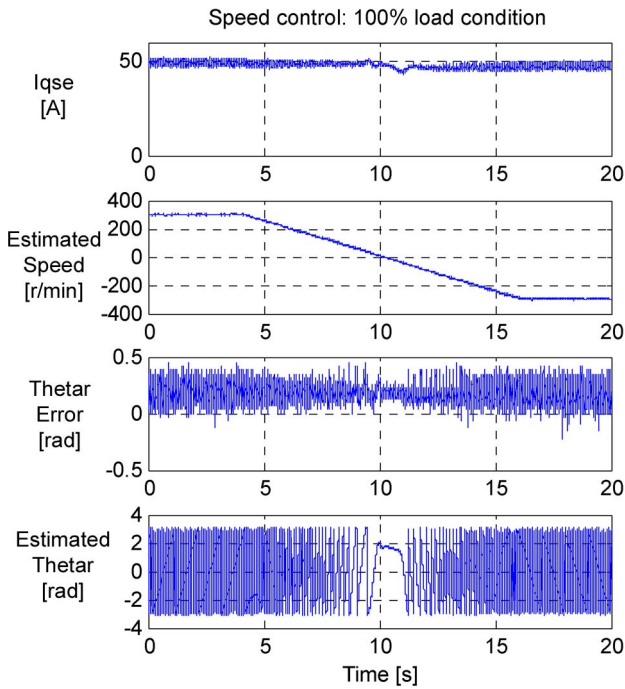
Fig. 18. Speed control from 300 to −300 r/min with full load. *q*-axis current, estimated speed, position error, and estimated rotor position.

even though, at the zero speed, the speed was regulated smoothly. In the 100% load condition, the speed was controlled slowly from 300 to −300 r/min, as shown in Fig. 18. The position estimation error varied from 0 to 0.4 rad, and the average error is about 0.2 rad. This offset position error can be further decreased by compensation of the average value according to the load condition [24]. In Figs. 17 and 18, there are some oscillations in the position errors, which are by the spatial harmonics in the inductances. Fig. 19 shows the speed control results of sinusoidal speed references, 5 and 25 Hz, respectively. The real speed was measured by the encoder for monitoring purpose, and the feedback signal to the speed control loop was the estimated speed by the sensorless control method. With the 5-Hz sinusoidal speed reference, the speed was estimated and controlled exactly. Moreover, with the 25-Hz sinusoidal speed reference, the speed was estimated well, and the estimated speed, as well as the real monitored speed, showed the 45° phase delay to its reference. From the figure, it can be concluded that the bandwidth of the speed control loop based on the proposed sensorless control is around 25 Hz.

Fig. 20 shows the position control performance. The electric rotor position varied from −2 to 2 rad, which means that the mechanical rotor position is from −2/3 to 2/3 rad because the pole pair of the IPMSM under test is three. With 25% and 70% load conditions, the electric rotor position error is less than 0.3 rad, which means less than 0.1-rad error in mechanical angle without any position compensation. Fig. 20(c) shows the position control result with the step load condition. Because of the torque control bandwidth, the rotor position varied due to the step load. However, the estimated rotor position tracked the real rotor position exactly. The electric position error between the estimated position and the real position was demonstrated in Fig. 20(c). In Fig. 20, the position error differs according
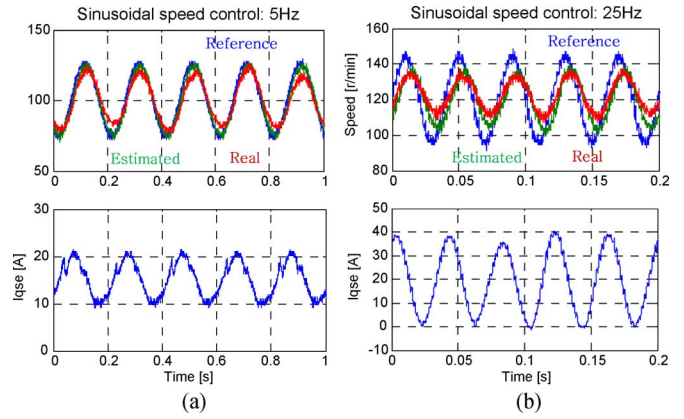

Fig. 19. Speed control performance with sinusoidal speed reference. Speed reference, estimated speed, real speed, and *q*-axis current are displayed. (a) 5-Hz sinusoidal speed reference. (b) 25-Hz sinusoidal speed reference.
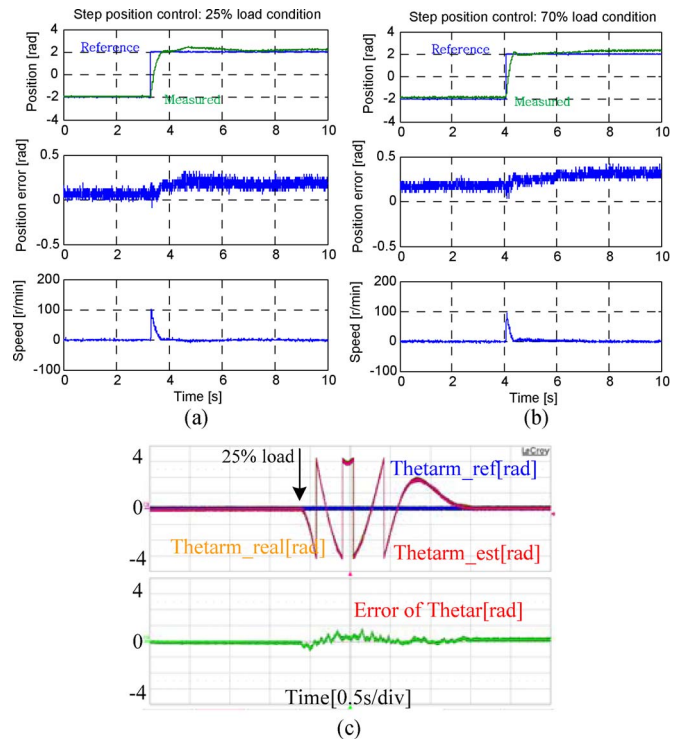

Fig. 20. Electric rotor position control. Electric rotor position reference varied from −2 to 2 rad. (a) 25% load condition. (b) 70% load condition. (c) 25% step load: Mechanical position reference, estimated position, real position, and electrical position error between the estimated and the real position.

to the rotor position even with the constant load condition. This difference is caused by the spatial harmonics in the inductances.

Due to the 16-kHz high injection frequency, the acoustic noises could be reduced immensely. However, the increased frequency signal causes the side effect: loss increase. Generally, the core loss increases according to the frequency of the current signal. Fig. 21 shows the temperature of the machine in the 5- and 16-kHz signal injections, respectively. In the case of the 16-kHz signal injection, the saturated temperature is higher than that of the 5-kHz signal injection.
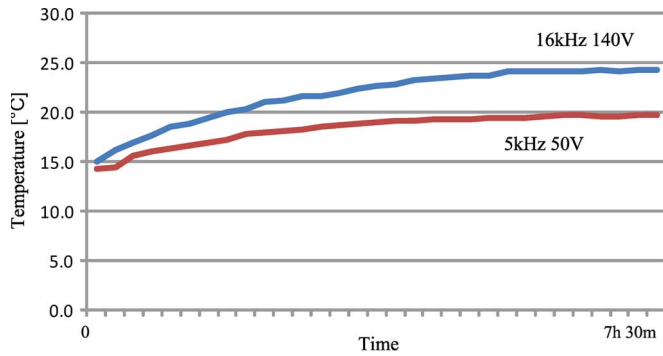
Fig. 21.　Machine temperature in 5- and 16-kHz pulsating signal injections.

IV. CONCLUSION

This paper has presented a method to inject high-frequency signal, whose frequency is the same as the PWM switching frequency of the inverter, for the position sensorless drive of an IPMSM. To extract the information regarding the rotor position, the current ripple components according to the injected voltage signal are used. The differences between successively sampled currents are used for the demodulation process, and neither LPF nor bandpass filter is necessary in the process. To inject the PWM switching frequency into IPMSM, the injected voltage signal was synchronized with a PWM carrier wave. Because of this high injection frequency, the dynamics of the sensorless control can be enhanced. The proposed method can be applied to both the stationary reference frame injection, the so-called rotating signal injection, and to the estimated rotor reference frame injection, the so-called pulsating signal injection. Through the experimental results obtained at 5- and 16-kHz PWM switching frequencies, the current control performances, the speed control performances, and the position control performances were demonstrated with the 11-kW off-the-shelf general-purpose IPMSM. In particular, the audible noise was virtually eliminated with the 16-kHz PWM switching frequency. The bandwidth of the speed control loop was evaluated through the sinusoidal speed reference test, and it concluded that the bandwidth is around 25 Hz. Also, the accuracy of the position control is within 0.1 rad in mechanical angle regardless of the load variation. Based on the speed control and position control performance with virtually eliminated acoustic noise, the proposed sensorless control can replace the position sensor of the low-end servo with position sensor in near future.

REFERENCES

[1] N. Bianchi and T. M. Jahns, "Design, analysis, and control of interior PM synchronous machines," in *Tutorial Course Notes IEEE IAS Annu. Meeting*, Seattle, WA, Oct. 3–7, 2004, pp. 1.1–1.10.

[2] P. Vas, *Sensorless Vector and Direct Torque Control*. New York: Oxford Univ. Press, 1998, pp. 122–124.

[3] J.-I. Ha, K. Ide, T. Sawa, and S.-K. Sul, "Sensorless rotor position estimation of an interior permanent-magnet motor from initial states," *IEEE Trans. Ind. Appl.*, vol. 39, no. 3, pp. 761–767, May/Jun. 2003.

[4] N. Matsui, "Sensorless operation of brushless dc motor drives," in *Proc. IEEE IECON*, 1993, pp. 739–744.

[5] S. Morimoto, K. Kawamoto, M. Sanada, and Y. Takeda, "Sensorless control strategy for salient-pole PMSM based on extended EMF in rotating reference frame," *IEEE Trans. Ind. Appl.*, vol. 38, no. 4, pp. 1054–1061, Jul./Aug. 2002.

[6] B.-H. Bae, S.-K. Sul, J.-H. Kwon, and J.-S. Byeon, "Implementation of sensorless vector control for super-high-speed PMSM of turbo-compressor," *IEEE Trans. Ind. Appl.*, vol. 39, no. 3, pp. 811–818, May/Jun. 2003.

[7] A. B. Kulkarni and M. Ehsani, "A novel position sensor elimination technique for the interior permanent-magnet synchronous motor drive," *IEEE Trans. Ind. Appl.*, vol. 28, no. 1, pp. 144–170, Jan./Feb. 1992.

[8] S. Ogasawara and H. Akagi, "Implementation and position control performance of a position-sensorless IPM motor drive system based on magnetic saliency," *IEEE Trans. Ind. Appl.*, vol. 34, no. 4, pp. 806–812, Jul./Aug. 1998.

[9] M. Mamo, K. Ide, M. Sawamura, and J. Oyama, "Novel rotor position extraction based on carrier frequency component method (CFCM) using two reference frames for IPM drives," *IEEE Trans. Ind. Electron.*, vol. 52, no. 5, pp. 508–514, Apr. 2005.

[10] V. Petrovic, A. M. Stankovic, and V. Blasko, "Position estimation in salient PM synchronous motors based on PWM excitation transients," *IEEE Trans. Ind. Appl.*, vol. 39, no. 3, pp. 835–843, May/Jun. 2003.

[11] M. Schroedl, "Sensorless control of ac machine at low speed and standstill based on the "INFORM" method," in *Conf. Rec. IEEE IAS Annu. Meeting*, 1996, pp. 270–277.

[12] P. L. Jansen and R. D. Lorenz, "Transducerless position and velocity estimation in induction and salient ac machines," *IEEE Trans. Ind. Appl.*, vol. 31, no. 2, pp. 240–247, Mar./Apr. 1995.

[13] M. J. Corley and R. D. Lorenz, "Rotor position and velocity estimation for a salient-pole permanent magnet synchronous machine at standstill and high speeds," *IEEE Trans. Ind. Appl.*, vol. 34, no. 4, pp. 784–789, Jul./Aug. 1998.

[14] J.-I. Ha and S.-K. Sul, "Sensorless field-orientation control of an induction machine by high-frequency signal injection," *IEEE Trans. Ind. Appl.*, vol. 35, no. 1, pp. 45–51, Jan./Feb. 1999.

[15] R. Leidhold and P. Mutschler, "Improved method for higher dynamics in sensorless position detection," in *Proc. IEEE IECON*, 2008, pp. 1240–1245.

[16] Y.-D. Yoon, S.-K. Sul, S. Morimoto, and K. Ide, "High bandwidth sensorless algorithm for ac machines based on square-wave-type voltage injection," *IEEE Trans. Ind. Appl.*, vol. 47, no. 3, pp. 1361–1370, May/Jun. 2011.

[17] R. Masaki, S. Kaneko, M. Mombu, T. Sawada, and S. Yoshihara, "Development of a position sensorless control system on an electric vehicle driven by a permanent magnet synchronous motor," in *Proc. IEEE PCC*, Osaka, Japan, 2002, vol. 2, pp. 571–576.

[18] S. Kim, Y.-C. Kwon, S.-K. Sul, J. Park, and S.-M. Kim, "Position sensorless operation of IPMSM with near PWM switching frequency signal injection," in *Proc. ICPE ECCE Asia*, Jeju, Korea, 2011.

[19] F. Briz, M. W. Degner, P. Garcia, and R. D. Lorenz, "Comparison of saliency-based sensorless control techniques for ac machines," *IEEE Trans. Ind. Appl.*, vol. 40, no. 4, pp. 1107–1115, Jul./Aug. 2004.

[20] F. Briz, M. W. Degner, A. Diez, and R. D. Lorenz, "Static and dynamic behavior of saturation-induced saliencies and their effect on carrier-signal-based sensorless ac drives," *IEEE Trans. Ind. Appl.*, vol. 38, no. 3, pp. 670–678, May/Jun. 2002.

[21] D.-W. Chung, J.-S. Kim, and S.-K. Sul, "Unified voltage modulation technique for real-time three-phase power conversion," *IEEE Trans. Ind. Appl.*, vol. 34, no. 2, pp. 374–380, Mar./Apr. 1998.

[22] S. Bolognani, S. Calligaro, R. Petrella, and M. Tursini, "Sensorless control of IPM motors in the low-speed range and at standstill by HF injection and DFT processing," *IEEE Trans. Ind. Appl.*, vol. 47, no. 1, pp. 96–104, Jan./Feb. 2011.

[23] H. Kim and R. D. Lorenz, "Carrier signal injection based sensorless control methods for IPM synchronous machine drives," in *Conf. Rec. IEEE IAS Annu. Meeting*, 2004, pp. 977–984.

[24] J.-I. Ha, "Analysis of inherent magnet position sensors in symmetric ac machines for zero or low speed sensorless drives," *IEEE Trans. Magn.*, vol. 44, no. 12, pp. 4689–4696, Dec. 2008.
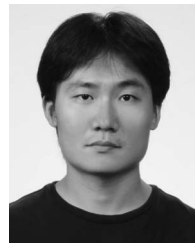
Sungmin Kim (S'09) was born in Seoul, Korea, in 1980. He received the B.S. and M.S. degrees in electrical engineering from Seoul National University, Seoul, in 2002 and 2008, respectively, where he is currently working toward the Ph.D. degree.

His current research interests are power electronics control of electric machines, sensorless drives, matrix converter drives, and power conversion circuits.

Jung-Ik Ha (S'97–M'01) was born in Korea in 1971. He received the B.S., M.S., and Ph.D. degrees in electrical engineering from Seoul National University, Seoul, Korea, in 1995, 1997, and 2001, respectively.

From 2001 to 2002, he was a Researcher with YASKAWA Electric Corporation, Japan. From 2003 to 2008, he worked for SAMSUNG Electronics Company, Korea, as a Senior and Principal Engineer. From 2009 to 2010, he was Chief Technology Officer with LS Mecapion Company, Korea. Since 2010, he has been an Assistant Professor in the School of Electrical Engineering, Seoul National University. His research interests include circuits and control in high-efficiency and integrated electric energy conversions for various industrial fields.

Seung-Ki Sul (S'78–M'80–SM'98–F'00) was born in Korea in 1958. He received the B.S., M.S., and Ph.D. degrees in electrical engineering from Seoul National University, Seoul, Korea, in 1980, 1983, and 1986, respectively.

From 1986 to 1988, he was an Associate Researcher in the Department of Electrical and Computer Engineering, University of Wisconsin, Madison. From 1988 to 1990, he was a Principal Research Engineer with Gold-Star Industrial Systems Company. Since 1991, he has been a member of the faculty of the School of Electrical Engineering, Seoul National University, where he is currently a Professor. From 2005 to 2007, he was the Vice-Dean of the College of Engineering, Seoul National University. From 2008 to 2011, he was the President of the Korea Electrical Engineering and Science Research Institute, Seoul. His current research interests are power-electronic control of electric machines, electric/hybrid vehicle drives, and power-converter circuits.